Finite volume discretization for dynamic viscosities on Voronoi grids

Christian Hüttig, Kai Stemmer

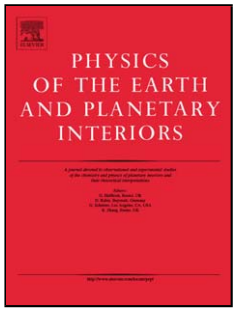

Title: Finite volume discretization for dynamic viscosities on Voronoi grids

Authors: Christian Hüttig, Kai Stemmer

PII: S0031-9201(08)00165-9
DOI: doi:10.1016/j.pepi.2008.07.007
Reference: PEPI 4996

To appear in: *Physics of the Earth and Planetary Interiors*

Received date: 15-11-2007
Revised date: 15-5-2008
Accepted date: 7-7-2008

Please cite this article as: Hüttig, C., Stemmer, K., Finite volume discretization for dynamic viscosities on Voronoi grids, *Physics of the Earth and Planetary Interiors* (2007), doi:10.1016/j.pepi.2008.07.007

Finite volume discretization for dynamic viscosities on Voronoi grids

Christian Hüttig[1] and Kai Stemmer, Institute of Planetary Research, Department of Planetary Physics, German Aerospace Center (DLR), Berlin, Germany

Abstract

We present a new formulation to discretize the viscous term in the momentum equation of the Navier-Stokes set. A technique based on the finite volume method enables thermal convection models to utilize spatially varying viscosity on a collocated variable arrangement. This technique can be applied to various grids in two or three dimensions with Voronoi properties, either irregular as the spiral grid or regular like the cubed sphere grid, icosahedral or simple boxes. A model for mantle convection implements this discretization and is compared to other published models. Further computational aspects are illuminated to efficiently reduce required resources.

1. Introduction

Over the last three decades, local discretization methods like finite-element (FE), finite-volume and finite-difference (FD) methods have firmly established themselves as the approach for computational fluid-flow problems in geophysics, especially with regard to thermal convection problems involving spatially varying viscosities in two (Parmentier, 1978; Christensen, 1984; Hansen and Yuen 1993; Solomatov and Moresi 2000) and three dimensions (Ogawa et al., 1991; Christensen and Harder 1991; Trompert and Hansen, 1998; Tackley 1998; Stein et al. 2004) as well as in spherical shells (Tabata and Suzuki, 2000; Zhong et al 2000; Yoshida and Kageyama 2004; McNamara and Zhong 2005; Choblet 2005; Stemmer et al. 2006). The advantages of irregular grids like arbitrary refinements and resolution choices were left outside because of more complicated discretization techniques and computational

[1] Corresponding Author

requirements. Nevertheless, these advantages become especially interesting in cases with complex geometries like spheres in three dimensions (3D) or disks in two dimensions (2D), which occur regularly in geophysics. This work demonstrates a technique to utilize the FV method on irregular grids in 3D with a focus on the spatial derivate of the stress tensor, required for the implementation of dynamic viscosities, which is of primary interest in the field of mantle convection modeling, e.g. Stemmer et al., 2006.

Most of the published models for mantle convection that include locally varying viscosities implement the necessary spatial derivative of the stress tensor with finite-elements (Zhong et al. 2000) or utilize grid-regularities (Yoshida and Kageyama 2004, Choblet 2005, Stemmer et al. 2006). Staggered approaches where velocity and scalar fields do not coincide at the same locations were preferred because of their straightforward implementation and elimination of numerical oscillations (Peric et al., 1988). Advantages of the FVM are the direct connection to the underlying physical problem and the conservative nature of its scheme that enables a direct implementation of boundary conditions similar to the finite-difference method. A disadvantage arises in irregular grids. The effort to discretize the desired equations with the FV method increases once the walls between the computational cells become tilted and spatial derivates besides the normal direction are required. Ferziger and Péric, 2001 describe an effective approach to acquire a correct solution for tilted walls. The only remaining problem within an irregular grid was the implementation of a spatial derivative of the relatively complex stress tensor that is required for locally varying viscosities in geophysical flow problems.

The approach presented in this paper bases on the proposed dual-grid approach in Ferziger and Péric, 2001. It utilizes a Voronoi grid as cellular discrete basis for the domain and its dual, the Delaunay triangulation to setup shape functions for an arbitrary linear interpolation mechanism (Baranger et al., 1996), as shown in figure 1. The triangulation in combination with a Voronoi discretization is able to fulfill all requirements for irregular grids in a FV

scheme. In recent years, computational and storage improvements have opened the door to embrace the use of complex grids with their advantages and increased computational requirements.

2. Numerical Method

2.1. Preface

The domain of interest in FV and FE methods is defined as control volumes, integrated over the governing differential equations of interest (Ferziger and Péric, 2001). Moving further to fluid mechanics, the basis of the FVM is therefore the integral form of the conservation equations. The solution domain is divided into a finite number of control volumes (CVs), and the conservation equations are applied to each CV. At the centroid of each CV lies a computational node at which the variable values are to be calculated. Interpolation is used to express variable values at the CV surface in terms of the nodal (CV-center) values. Surface and volume integrals are approximated using suitable quadrature formulae. As a result, one obtains an algebraic equation for each CV, in which a possible varying number of neighbor nodal values appear (Fletcher, 2001).

The FVM can accommodate any type of grid, so it is suitable for regular and irregular grids. Most regular grids are Voronoi grids by nature, which means that within a CV every point is closer to its associated nodal location than to any other. This nodal location serves as generator point for a Voronoi region and results in a CV. The resulting cell structure offers interesting properties: the face dividing two neighboring CVs lies always midway and perpendicular between them, which is one requirement for the FV method. The amount of faces is the direct count of neighbors for a specific CV and is always minimal (Okabe et al., 2000). This neighbor count is directly associated with the matrix column count per row.

Exploiting the detail that a face lies midway between two neighboring nodes reduces the difficulties of interpolating scalar values to the face centers, which is essential for the FV

method. To determine the face-value ϕ_f between the nodes *N1* and *N2* of a scalar ϕ, a central difference scheme (CDS) results in

$$\phi_f = \frac{1}{2}(\phi_{N1} + \phi_{N2}). \tag{1}$$

The CDS results in a second order accuracy as long as the interpolated point coincides with the center of the face. On condition that the mid-point stays within the face, the FVM has at least a first order accuracy (Ferziger and Péric, 2001). A complete FVM discretization with CDS interpolation for the Nabla operator, where *P* specifies a discrete node index, *N* the neighbor index and *PN* face quantities for the face between *P* and *N* like area *A* and normal vector $\vec{n}$ results in

$$\nabla\phi_P = \int_V \nabla\phi_P \, dV = \frac{1}{V_P}\int_S \phi_f \cdot \vec{n} \, dS = \frac{1}{V_P}\sum_N \phi_f A_{PN} \cdot \vec{n}_{PN}$$

$$= \frac{1}{V_P}\sum_N \frac{1}{2}(\phi_P + \phi_N) A_{PN} \cdot \vec{n}_{PN} \tag{2}$$

.

If ϕ is a vector, equation (2) reduces to the divergence operator *div(ϕ)*, for a scalar field the result is the gradient operator *grad(ϕ).*

2.2. Barycentric Interpolation

A more complex interpolation scenario arises for irregular grids. Faces often undergo a perpendicular shift that moves the face center away from the interpolated midpoint. To hold on to the second order accuracy, the necessity for a more complex interpolation arises.

An obvious choice is linear interpolation from a triangulated domain. Since the Delaunay triangulation is the dual of the Voronoi diagram (Okabe et al., 2000), utilizing it is straightforward. The barycentric coordinates (Shepard, 1968) offer a simple way to interpolate at any point within a triangulated domain. As they are coordinates, they provide position information relative to a simplex (*D* - dimensional tetrahedral region). As a side effect, these coordinates in a normalized homogeneous form (their sum equals one) provide weight information for the specified location, as Figure 2 illustrates. In contrast to the natural neighbor interpolation introduced by Sambridge et al., 1995, this method requires always a minimal amount (*D*+1) of nodal values and does not require recursive formulas to obtain the weights.

Correct interpolation to the center of the face *PN* is now possible and by the use of barycentric interpolation remains of second order accuracy (Ferziger and Péric, 2001, chapter 8.6). Equation (1) changes with the help of barycentric weights λ to

$$\phi^{fc} - \sum_{d=1}^{D+1} \lambda_d^w \phi_{\lambda_d^i} \quad , \tag{3}$$

where λ denotes the barycentric coordinates for a *D*-dimensional space, including the nodal indices λ^i of the according Delaunay simplex edge and the weight (or normalized coordinate) λ^w. Figure 3 illustrates all variables for the two-dimensional case within a single cell.

2.3. Spatial derivative of the deviatoric stress tensor

Many geophysical fluids require a spatial derivative of the stress tensor as part of the Navier-Stokes momentum equation. This enables the simulation to handle spatially varying viscosities. The definition of the deviatoric stress tensor of a velocity *u* and dynamic viscosity η is

$$\tau_{ij} = \eta\left(\frac{\partial u_i}{\partial x_j} + \frac{\partial u_j}{\partial x_i}\right) = \eta(\nabla\vec{u} + (\nabla\vec{u})^T) \tag{4}$$

and results therefore in a rank 2 symmetric tensor of *D*x*D* dimensions. It can be expressed as

components of gradients of velocity components as shown in equation (5) for the two-dimensional case, where the diagonal parts represent the normal stresses and the off-diagonal parts shear stresses:

$$\tau_{ij} = \eta \begin{bmatrix} 2(\nabla \vec{u}_x)_x & (\nabla \vec{u}_y)_x + (\nabla \vec{u}_x)_y \\ (\nabla \vec{u}_x)_y + (\nabla \vec{u}_y)_x & 2(\nabla \vec{u}_y)_y \end{bmatrix} \tag{5}$$

The spatial derivative of this tensor results in a vector and according to the FV scheme is

$$\nabla \cdot \tau = \int_V \nabla \cdot \tau \, dV = \frac{1}{V} \int_S \tau \, \vec{n} \, dS \tag{6}$$

For constant η, $\nabla \bullet \tau$ reduces to $\eta \nabla^2 \vec{u}$. The problem for the FV method arises now that the gradients of the velocity components are required at the faces. The literature describes several ways to approximate the normal component to implement the Laplacian operator ∇^2 (Ferziger and Péric 2001; Fletcher 1991). Usually finite difference schemes express derivatives at the faces. The problem with varying viscosities is that also at least one other non-normal spatial derivate is required. Stemmer et al., 2006 recently formulated an elegant solution for the regular cubed sphere grid for collocated variable arrangement, utilizing midpoint interpolation of neighboring nodes in several directions. This technique is useful for cubical grid-setups but fails on irregular grids.

Including the neighbors of a nodes neighbor would resolve this issue and guarantees second order accuracy, but also increases the solution matrix size dramatically and would therefore make this approach impractical. Another choice is a change to the finite-difference approach on the faces. With the help of shape functions from the barycentric coordinates (2.2), a Cartesian cross can be constructed from the center of a face. This enables an FD formulation at the faces as presented in figure 4. The FV integral for an arbitrary u_i would

evolve with the interpolation sources *fi+/-* as in equation (2) for the Cartesian interpolation cross and *fc* for the center as

$$\int_S \tau \cdot \vec{n}\, dS = \int_S \eta\left(\frac{\partial u_i}{\partial x_j} + \frac{\partial u_j}{\partial x_i}\right) \cdot \vec{n}\, dS = \sum_N \sum_{j=1}^{D} \frac{u_i^{fj+} - u_i^{fj-} + u_j^{fi+} - u_j^{fi-}}{d_s} \eta^{fc} A_{PN} \cdot \vec{n}_{PN}$$

, (7)

where d_S specifies the size of the interpolation cross. This distance can be either fixed for the whole grid or varying for every face, depending on resolution differences. It is untested what the optimal value for d_S is, but tests have shown that for a certain face area A_{PN} in a *D*-dimensional space $d_S = \sqrt[D-1]{A_{PN}}$ leads to a minimum of foreign neighbors (not depending on neither one of the original nodes that the face divides) on strongly irregular grids.

A different problem arises with the required viscosity at the cell face (η^{fc}). Assuming the viscosity is correct at the face center, the method guarantees through pure use of second order interpolants a second order truncation error. This might not hold true if the viscosity needs to be interpolated. For example, in regular grids it can be shown that the harmonic interpolant of viscosity between adjacent cells preserves continuity of the normal stress component resolved onto the face from cell-to-cell, which is closer to the physical truth of the situation. However, this does not necessarily hold true for continuity of shear stress, and suggests another viscosity interpolant might be used. An implementation of a dual stencil composed of shear and normal components of stress and their associated continuity could ensure a proper viscosity interpolant at the faces.

2.4. Laplacian

The energy conservation as well as the momentum conservation equation for constant viscosities consists of the Laplacian operator ∇^2. The FV discretization results in

$$\nabla^2\phi = \int_V \nabla^2\phi \, dV = \frac{1}{V}\int_S \nabla\phi \cdot \vec{n} \, dS \tag{8}$$

which requires the gradient in normal direction at the cell face. The fact that only the normal direction of the gradient is required can be exploited and replaced by a CDS (Fletcher 1991):

$$\int_S \nabla\phi \cdot \vec{n} \, dS = \sum_N \frac{\phi_N - \phi_P}{d_{PN}} A_{PN} \tag{9}$$

This approximation for the face stays second order accurate even in irregular grids since the derivative between *P* and *N* does not change within all simplexes that have both, *P* and *N*, as connectors. However, a face center can move out of those simplexes on strongly deformed cells. In this case, it is useful to introduce barycentric weights of the normal direction from the face center *fn+/-*, as illustrated in Figure 3 as well. Equation (9) changes to

$$\int_S \nabla\phi \cdot \vec{n} \, dS = \sum_N \frac{\phi^{fn+} - \phi^{fn-}}{d_S} A_{PN} \tag{10}$$

and guarantees second order accuracy for all Voronoi cells.

3. Computational Aspects and Tests

3.1. Setup phase

In order to utilize the in chapter two presented scheme, a pre-calculated Voronoi diagram and Delaunay triangulation for the same discrete set of points should exist with the following information:

- Nodal positions
- Cell volumes
- List of faces with their two neighbor indices (the node indices they divide), area and center

- List of simplex indices

The interpolation information for each face must exist and should be pre-calculated to run a simulation efficiently. They stay in a fixed position during the simulation and can therefore be pre-calculated. One set of interpolation information consists of a simplex index that in turn holds the *D*+1 nodal indices λ_d^i and weight information λ_w^i. Each face usually has 2*D*+3 or 2*D*+1 interpolation points consisting of the center, the Cartesian cross and two more depending on the use of the *fn+/-* weights as described in chapter 2.4.

To find a certain point within a Delaunay triangulation, it is possible to calculate the barycentric coordinates of a desired point relative to every simplex with equation (3) until each single coordinate lies between zero and one, as described in chapter 2.2. The time complexity of this procedure falls into $\mathrm{O}\left(n^2\right)$. To reduce this to $\mathrm{O}\left(n \log n\right)$, it is possible to index the simplex indices within a search tree. These indices correspond to node indices, which can be found in the face neighbor information as well. Since only locations close to a certain face are looked up, the simplexes containing the neighbor nodes of a face can be checked first. For extremely deformed cells, the fallback to a check-every-simplex should exist as well.

3.2. Storage requirements

Including the *fn+/-* weights, interpolation information for one face requires

$$(1+D)(3+2D)(W+I) \tag{11}$$

bytes if a weight is stored with *W* bytes and an index with *I* bytes. On an average irregular grid in three dimensions, one node contains of approx. 14 neighbors (Huettig and Stemmer 2006), resulting in 7*R* faces, where *R* denotes the total node count. Assuming further double floating-point precision for the weights (*W*=8) and standard 32-bit integer for indices (*I*=4), the total memory requirement for the interpolation information is 3024*R* byte.

To reduce this enormous extra memory requirement one can exploit the fact that a weight is always only in the range between zero and one. Utilizing fast integer arithmetic can turn a 16-bit integer into a floating point consisting of 2^{16} steps between zero and one, introducing a global error of $\frac{D+1}{2^{16}}$ and a reduction to W=2, resulting in 1512R byte. A reduction to I=3 is only theoretically possible because it leads, if even possible, practically to misaligned memory that dramatically reduces performance.

3.3. Validation

In order to test the presented numerical technique several results from other published mantle convection models were reproduced to verify its accuracy. According to linear stability analysis (Busse, 1975), there are two stable solutions for thermal convection in the three-dimensional spherical shell with an inner to outer radius ratio of 0.55 that is comparable to the Earth's mantle and is purely bottom heated. The complete set of equations is

217

$$\nabla \cdot \boldsymbol{u} = 0$$

218

$$\frac{\partial T}{\partial t} + \boldsymbol{u}\nabla T - \nabla^2 T = 0$$

219

$$\nabla \cdot \left[\eta\left(\nabla \boldsymbol{u} + (\nabla \boldsymbol{u})^T\right)\right] + Ra\, T\, \boldsymbol{e}_r - \nabla p = 0$$

$$\eta(T) = \exp(\gamma(T_{ref} - T) \qquad Ra = \frac{\rho g \alpha \Delta T d^3}{\kappa \eta_{ref}} \qquad \eta_{ref} = \eta(T_{ref})$$

220

221 , where *T* is the Temperature, ***u*** the velocity, *p* the hydrostatic pressure, *t* the time and e_r the
222 unity vector towards the gravitational center. The viscosity follows an Arrhenius law and is
223 purely temperature dependent, as in Stemmer et al., 2006.

224 The stationary stable flow patterns in tetrahedral and cubic symmetry are suitable to
225 compare output values like the heat flow at the core-mantle boundary and the volume-
226 averaged rms-velocity against other published models that use different discretization
227 schemes and numerical techniques. To initiate these steady state patterns, the initial conduc-
228 tive temperature field is perturbed with a normalized spherical harmonic mode Y_l^m with
229 small amplitude. The mode Y_3^2 forces a tetrahedral flow pattern and $Y_4^0 + Y_4^4$ results in a
230 cubical symmetric flow. A convergence test for an isoviscous tetrahedral flow with a Rayleigh
231 number of 7000 similar to the published test by Stemmer et al., 2006, results in the bottom
232 Nusselt numbers (3.3105, 3.4514, 3.4848, 3.4897) for a radial/lateral grid resolution of
233 (8/642, 16/2562, 32/10242, 48/10242) nodes. Table 1 shows a detailed comparison to other
234 published models of isoviscous convection $\Delta\eta T = 1$ and convection with temperature de-
235 pendent viscosity of $\Delta\eta T = 10$, $\Delta\eta T = 20$ and $\Delta\eta T = 30$ respectively as an extension to the
236 published results by Stemmer et al., 2006.

237 For the advection-diffusion equation of temperature a similar discretization approach
238 as described in 2.4 with a three-level implicit time stepping and a BiCGStab solver turned out
239 to be an efficient combination. A major advantage of the method discussed here lies in its
240 robustness for a fully implicit treatment: instead of a classical use of the Courant-criteria

241 which restricts the time step length on the maximal velocity within the system, an approach
242 utilizing the maximal difference in a velocity compared to the previous inner iteration lead to
243 equally good results. An effect of this restriction is that less chaotic convection models re-
244 quire less time steps and therefore computational time. Of course, on very turbulent models,
245 the difference is less pronounced and the computing time required for a single time step
246 becomes relatively large.

247 Table 2 shows, besides a more detailed comparison of local values such as radial min
248 / max velocities and temperatures at mid-depth, the computational effort for these kind of
249 problems. This table shows also the volatile nature of these control values as two different
250 initial conditions are compared to each other.

251 Figure 5a and b shows detailed flow patterns and temperature distributions of the te-
252 trahedral and cubical steady state pattern with low temperature dependent viscosity
253 ($\Delta\eta T$=20). Once $\Delta\eta T$ reaches a certain limit, the convective regime changes to stagnant-lid
254 convection. This transition is smooth and between contrasts of $\Delta\eta T$=1e4 and 5e5, as further
255 examined in three-dimensional spherical geometry by Stemmer et al., 2006. The here intro-
256 duced method shows the same behavior around this contrast and develops a stagnant lid, as
257 illustrated in figure 5c. Figure 6 displays the typical plume-thinning phenomena caused by
258 temperature dependent viscosity (Ratcliff et al. 1996; Hansen and Yuen, 1993). If the viscos-
259 ity contrast based on temperature is increased for a tetrahedral or cubical mode with mod-
260 erate Rayleigh numbers, the plume-tail gets thinner and faster.

261 ## 4. Summary

262 The discretization method presented in chapter 2 is a proof of concept for mantle
263 convection simulations in irregular n-dimensional grids. The spatial derivative of the stress
264 tensor offers further thermal convection models the possibility to utilize varying viscosities.
265 The discretization bases on the finite volume method and the dual-grid approach (Ferziger

and Péric, 2001). A Voronoi diagram is constructed around the locations of the nodes that act as cells for the control volumes. Furthermore, the dual of the Voronoi diagram, the Delaunay triangulation, serves as interpolation basis for values between the cells.

Chapter 3 illuminates computational aspects dealing with an effective way to store certain information within a setup phase and demonstrates how to reduce the extra resource requirements for this kind of discretization. There is also a hint on how to speed up the setup phase, reducing the time complexity back to $\mathrm{O}(n \log n)$.

A comparison with other published models for mantle convection validates the scheme and concludes this document. The verification bases on isoviscous and weakly temperature dependent steady state flow patterns in a bottom heated three-dimensional spherical shell with an aspect ratio of 0.55. Bottom heat flow (Nusselt number) and RMS velocity are compared to a collection of other published models of the same kind and shows promising results. The accuracy stays below two percent to other published values. The volatile nature of local control values to initial conditions is also demonstrated in table 2.

Another general advantage of this technique is the physical view on the problem. As Fletcher, 1991 noted, an advantage of the Finite Volume method is the direct view on the underlying physical problem without the need for higher order abstractions as required for a finite element approach, while maintaining its robustness and versatility.

Acknowledgements

The authors thank John Hernlund, David Yuen, and Paul Meakin for thoughtful and constructive reviews. The authors would also like to thank D. Breuer and T. Spohn of the German Aerospace Center (DLR) for providing the facilities utilized during this study. This work was carried out under the HPC-EUROPA project (RII3-CT-2003-506079), with the support of the European Community - Research Infrastructure Action of the FP6.

Baranger, J., Matre, J.F., Oudin, F.,1996. Connection between finite volume and mixed finite element methods, Math. Mod. Numer. Anal. 30 (4) 445--465.

Bercovici, D., Schubert, G., Glatzmaier, G.A., 1989. Threedimensional spherical models of convection in the Earth's mantle. Science 244, 950–955.

Blankenbach, B., Busse, F., Christensen, U., Cserepes, L., Gunkel, D., Hansen, U., Harder, H., Jarvis, G., Koch, M., Marquart, G., Moore, D., Olson, P., Schmeling, H., Schnaubelt, T., 1989. A benchmark comparison for mantle convection codes. Geophys. J. Int. 98, 23–38.

Busse, F.H., 1975. Patterns of convection in spherical shells. J. Fluid Mech. 72, 67–85.

Busse, F.H., Christensen, U., Clever, R., Cserepes, L., Gable, C., Giannan-drea, E., Guillou, L., Houseman, G., Nataf, H.-C., Ogawa, M., Parmentier, M., Sotin, C., Travis, B., 1993. 3D convection at infinite Prandtl number in Cartesian geometry—a benchmark comparison. Geophys. Astro. Fluid 75, 39–59.

Choblet, G., 2005. Modelling thermal convection with large viscosity gradients in one block of the 'cubed sphere'. J. Comput. Phys. 205, 269–291.

Christensen, U., 1984. Convection with pressure- and temperaturedependent non-Newtonian rheology. Geophys. J. R. Astro. Soc. 77, 343–384.

Christensen, U., Harder, H., 1991. 3D convection with variable viscosity. Geophys. J. Int. 104, 213–226.

Ferziger, J.H., Peric, M., 2001. Computational Methods for Fluid Dynamics, 3rd rev. ed. Edition, Springer, Berlin.

Fletcher, C.A.J., 1991. Computational Techniques for Fluid Dynamics, vol. 2., second ed. Springer, Berlin.

Hansen, U., Yuen, D.A., 1993. High Rayleigh number regime of temperature-dependent viscosity convection and the Earth's early thermal history. Geophys. Res. Lett. 20, 2191.

Harder, H., 1998. Phase transitions and the three-dimensional planform of thermal convection in the Martian mantle. J. Geophys. Res. 103, 16775–16797.

Harder, H., Hansen, U., 2005. A finite-volume solution method for thermal convection and dynamo problems in spherical shells. Geophys. J. Int. 161, 522–532.

Huettig, C., Stemmer, K., 2007. The spiral grid: A new approach to discretize the sphere and its application to mantle convection. Geochem. Geophys. Geosyst., in press

Iwase, Y., 1996. Three-dimensional infinite Prandtl-number convection in a spherical shell with temperature-dependent viscosity. J. Geomag. Geoelectr. 48, 1499–1514.

McNamara, A.K., Zhong, S., 2005. Degree-one mantle convection: dependence on internal heating and temperature-dependent rheology. Geophys. Res. Lett. 32, L01301.

Ogawa, M., Schubert, G., Zebib, A., 1991. Numerical simulations of three-dimensional thermal convection in a fluid with strongly temperature-dependent viscosity. J. Fluid Mech. 233, 299–328.

Okabe, A., Boots, B., Sugihara, K., Chiu, S.K., 2000. Spatial Tessellations: Concepts and Applications of Voronoi Diagrams, Wiley, ISBN 0471986356

Parmentier, E.M., 1978. A study of convection in non-Newtonian fluids. J. Fluid Mech. 84, 1–11.

Peric, M.,Kessler, R., Scheurer, G., 1988. Comparison of finite-volume numerical methods with staggered and colocated grids. Comp. Fluids 16, 389–403.

Ratcliff, J.T., Schubert, G., Zebib, A., 1996. Effects of temperaturedependent viscosity on thermal convection in a spherical shell. Physica D 97, 242–252.

Sambridge, M., Braun, J., McQueen, H., 1995. Geophysical parametrization and interpolation of irregular data using natural neighbours. Geophysical Journal International, 122 (3), pp. 837-857.

Shepard, D., 1968. Two- dimensional interpolation function for irregularly- spaced data, Proc 23rd Nat Conf, pp. 517-524

Stein, C., Schmalzl, J., Hansen, U., 2004. The effect of rheological parameters on plate behaviour in a self-consistent model of mantle convection. Phys. Earth Planet. Int. 142, 225–255.

Tabata, M., Suzuki, A., 2000. A stabilized finite element method for the Rayleigh-benard equations with infinite Prandtl number in a spherical shell. Comput. Methods Appl. Mech. Eng. 190, 387–402.

Tackley, P.J., 1998. Self-consistent generation of tectonic plates in three-dimensional mantle convection. Earth Planet Sci. Lett. 157, 9–22.

Trompert, R.A., Hansen, U., 1996. The application of a finite volume multi-grid method to three-dimensional flow problems in highly viscous fluids with a variable viscosity. Geophys. Astro. Fluid 83, 261–291.

Trompert, R.A., Hansen, U., 1998. Mantle convection simulations with rheologies that generates plate-like behaviour. Nature 395, 686–689.

Yoshida, M., Kageyama, A., 2004. Application of the Ying–Yang grid to a thermal convection of a Boussinesq fluid with infinite Prandtl number in a three-dimensional spherical shell. Geophys. Res. Lett. 31, L12609.

Zhong, S., McNamara, A., Tan, E., Moresi, L., Gurnis, M., 2008. A Benchmark Study on Mantle Convection in a 3-D Spherical Shell Using CitcomS. Submitted to G^3 on April 4, 2008.

358 Zhong, S., Zuber, M.T., Moresi, L., Gurnis, M., 2000. Role of temperature-dependent viscosity
359 and surface plates in spherical shell models of mantle convection. J. Geophys. Res. 105,
360 11063–11082.

Figure 1 shows the Voronoi diagram in red and the according Delaunay triangulation in blue for a random set of generator points

Figure 2 illustrates the barycentric coordinates for a point P within the triangle ABC.

Figure 3: A node P surrounded by its neighbors N, with the associated Voronoi diagram in red and the Delaunay triangulation in blue. The difference between the true face center with its barycentric coordinates λ and the central difference scheme (mid-point) is highlighted as well as important components for the FVM such as area A, distance d and normal vector $\vec{n}$.

Figure 4 shows as an extension to figure 3 the barycentric coordinates of the constructed Cartesian cross around the face center and the two interpolation points along the normal path of a pre-defined size d_S.

Figure 5 shows different convection patterns for a selected set of cases. All views display temperature, while the upper left part shows the residual iso-surface of temperature with the respective iso-values printed below, with a cutout of the positive domain for a better insight. The upper right part displays a slice with streamlines and the lower part a projection of the annotated shell. All cases are purely bottom heated with free-slip boundary conditions and purely temperature dependent viscosity variations. $Ra_{0.5}$=7000 in all cases. The different cases illustrate: a) $\Delta\eta T$=20, tetrahedral initial condition, b) $\Delta\eta T$=20, cubical initial condition, c) $\Delta\eta T$=1e6, random initial condition. Case c shows a similar pattern on all other initial conditions.

Figure 6 illustrates the difference of a weakly temperature dependent case ($\Delta\eta T$=20) with $Ra_{0.5}$=7000 to the isoviscous case. While a, b, c and e display the difference in velocity, d shows the difference in temperature. Because the slice views d and e are not centered around zero, they contain an extra red contour line.

Table 1: Comparison of the bottom Nusselt number and the rms-velocity for the tetrahedral and cubic steady-state convection with a viscosity contrast of $\Delta\eta T$=1, $\Delta\eta T$=20 and $\Delta\eta T$=30. The Rayleigh number is 7000 for T=0.5. The abbreviation 'Be89' stands for the results from Bercovici et al. (1989), 'Zh00' from Zhong et al. (2000), 'Iw96' from Iwase (1996), 'TS00' from Tabata and Suzuki (2000), 'Ha98' from Harder (1998), 'Ra96' from Ratcliff (1996) and 'YK04' from Yoshida and Kageyama (2004). The respective discretization method is listed as well, where 'SP' denotes spectral, 'FE' finite elements, 'FD' finite differences and 'FV' finite volumes.

Table 2 shows a comparison of global and local quantities as well as compute time measurements for some selected cases. The sole influence on the initial condition (I.C.) in the first two cases demonstrates the volatile nature of these values. All computations took place on an 8 CPU shared memory machine (Opteron 875 w/ 2.2GHz), while t_{CPU} shows the compute time in hours until an adequate steady state was reached. This final time is shown as non-dimensional diffusion time t, combined with n_{Iter} time steps. The grid consisted in all computations of a projected icosahedron with 32 radial levels and 10.242 lateral nodes. Other values consist of volume averaged temperature <T> and velocity <V>, as well as their interior (mid-shell) minima and maxima. The velocity minima and maxima are taken only from the radial component. Values in square brackets are from Zhong et al., 2008 and round brackets from Stemmer et al., 2006.

Tetrahedral symmetry			$\Delta\eta T = 1$		$\Delta\eta T = 10$		$\Delta\eta T = 20$	
Model	Method	Nodes	Nu_{T0}	v_{rms}	Nu_{T0}	v_{rms}	Nu_{T0}	v_{rms}
Be89	SP	2400	3.4657	-	-	-	-	-
Zh00	FE	165888	3.519	-	-	-	-	-
Iw96	FV	532480	3.45	32.4173	-	-	-	-
TS00	FE	324532	3.6565	32.936	-	-	-	-
Ha98	SP	552960	3.4955	32.6375	-	-	-	-
Ra96	FV	200000	3.4423	32.19	3.2337	26.80	3.1615	25.69
YK04	FD	2122416	3.4430	32.0481	-	-	3.133	26.1064
St06	FV	663552	3.4864	32.5894	3.2398	27.2591	3.1447	25.7300
This	FV	327744	3.4848	32.6535	3.2346	27.2513	3.1444	25.7139
Cubic symmetry			$\Delta\eta T = 1$		$\Delta\eta T = 20$		$\Delta\eta T = 30$	
Ha98	SP	552960	3.6086	31.0765	-	-	-	-
Ra96	FV	200000	3.5806	30.87	3.3663	25.17	3.3285	24.57
YK04	FD	2122416	3.5554	30.5197	3.3280	25.3856	-	-
St06	FV	663552	3.5982	31.0226	3.3423	24.9819	3.2864	24.1959
This	FV	327744	3.5953	31.0704	3.3315	24.9496	3.2747	24.1568

$Ra_{0.5}$	I.C.	$\Delta\eta T$	t	n_{iter}	t_{CPU}	Nu_t	Nu_b	<T>	$T_{i,min}$	$T_{i,max}$	<V>	$V_{ri,min}$	$V_{ri,max}$
1e5	Cubic	1	0.688 [0.315]	2110 [35000]	35.85	7.873 [7.850]	7.890 [7.770]	0.1826 [0.1728]	0.0304 [0.0228]	0.8804 [0.9454]	154.64 [154.8]	-265.58 [-261.5]	979.28 [982.6]
1e5	Random	1	0.748	1660	36.35	7.524 (7.371)	7.514 (7.372)	0.2493 (0.1941)	0.0306 (0.0271)	0.7970 (0.8973)	163.64 (153.13)	-396.70 (-275.65)	764.33 (949.34)
7000	Tetra	100	2.046 [2.0]	113 [30000]	3.33	2.909 [2.935]	2.920 [2.929]	0.2595 [0.2653]	0.0318 [0.0332]	0.9105 [0.9255]	23.13 [23.11]	-10.45 [-10.74]	166.59 [171.3]
7000	Tetra	1e3	1.001 [1.5]	201 [31000]	3.65	2.526 [2.546]	2.532 [2.535]	0.3027 [0.3124]	0.0662 [0.0695]	0.9292 [0.9452]	22.36 [22.90]	-6.40 [-6.97]	215.03 [226.7]

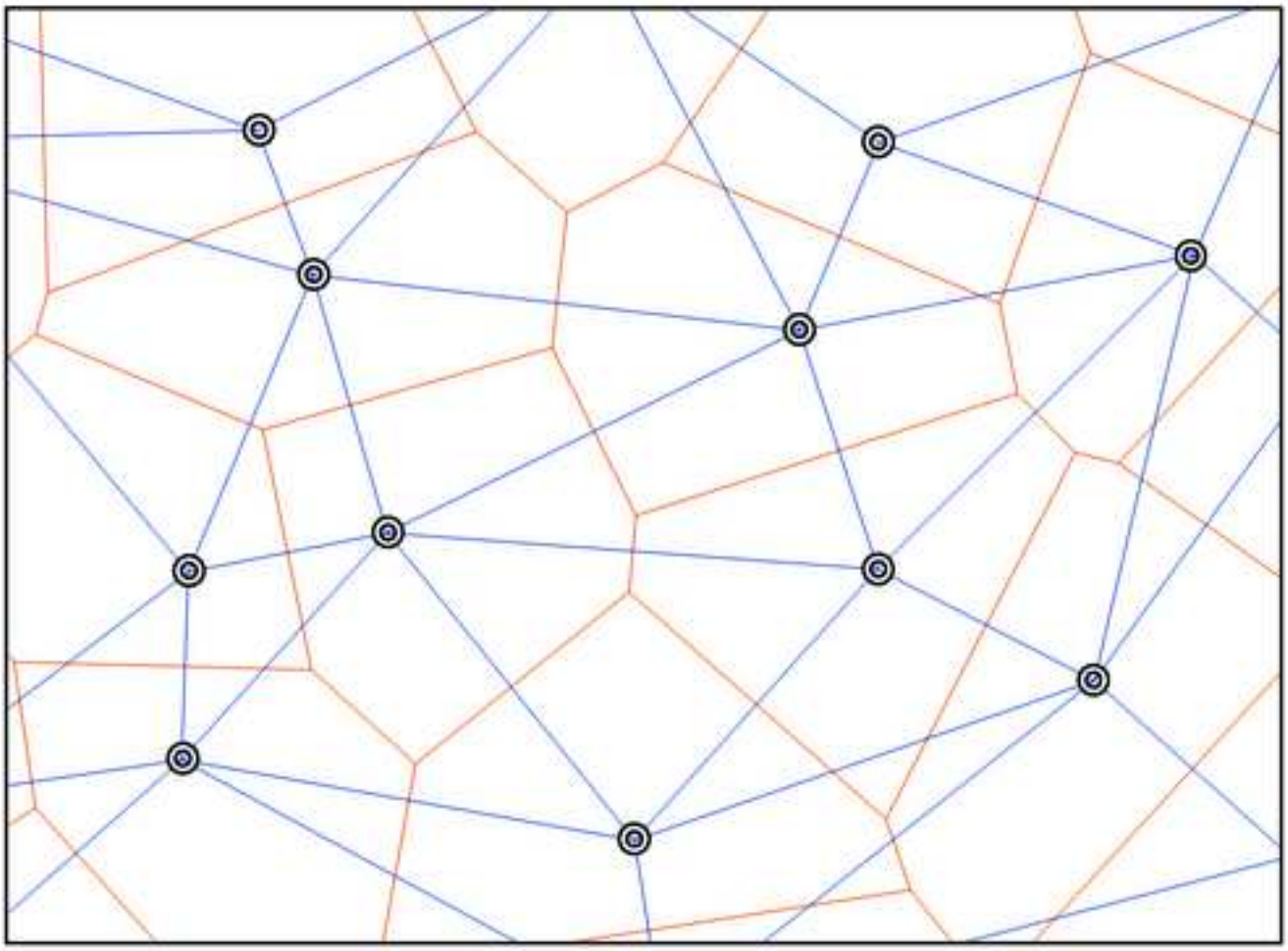

Figure 2

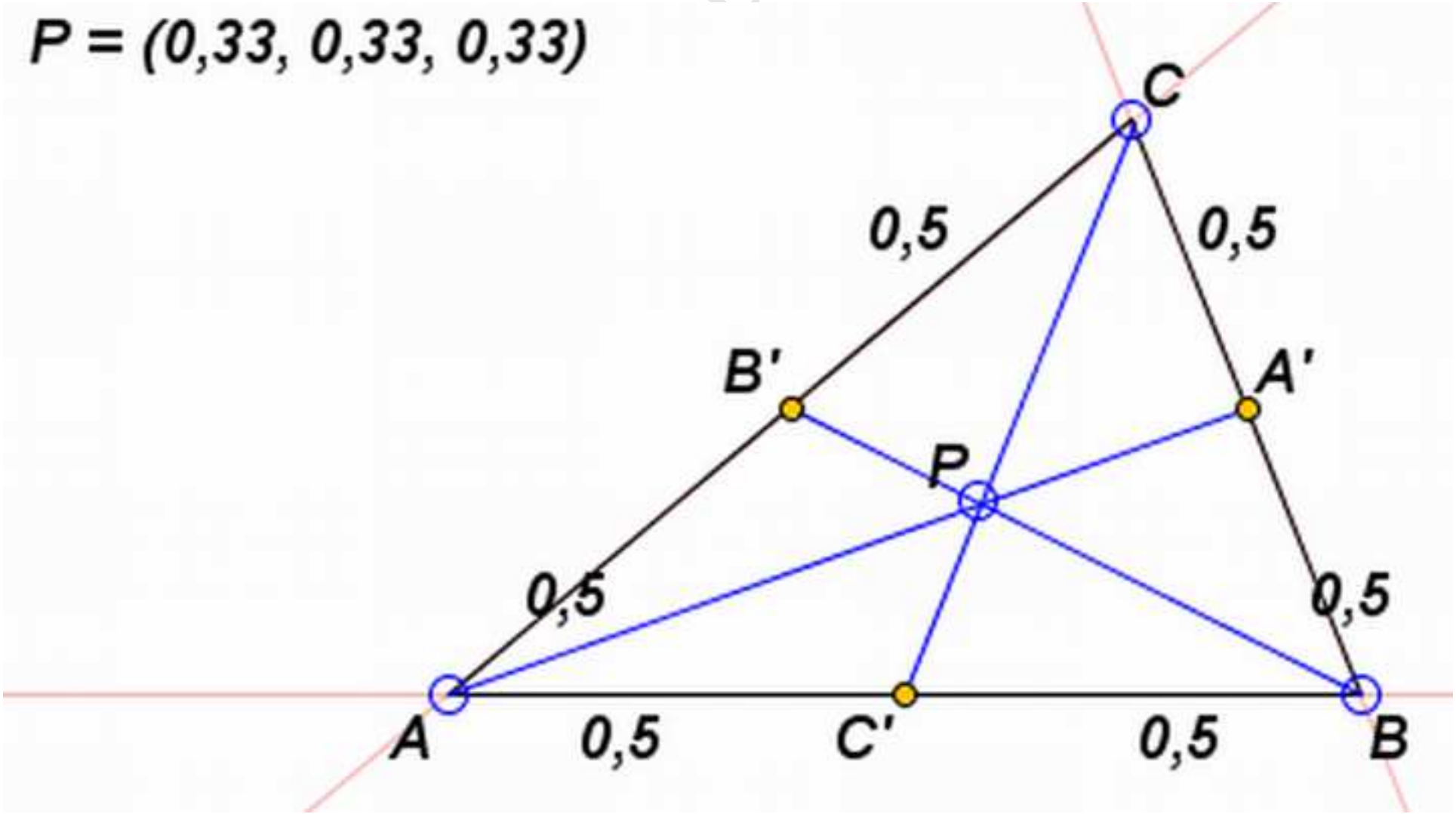

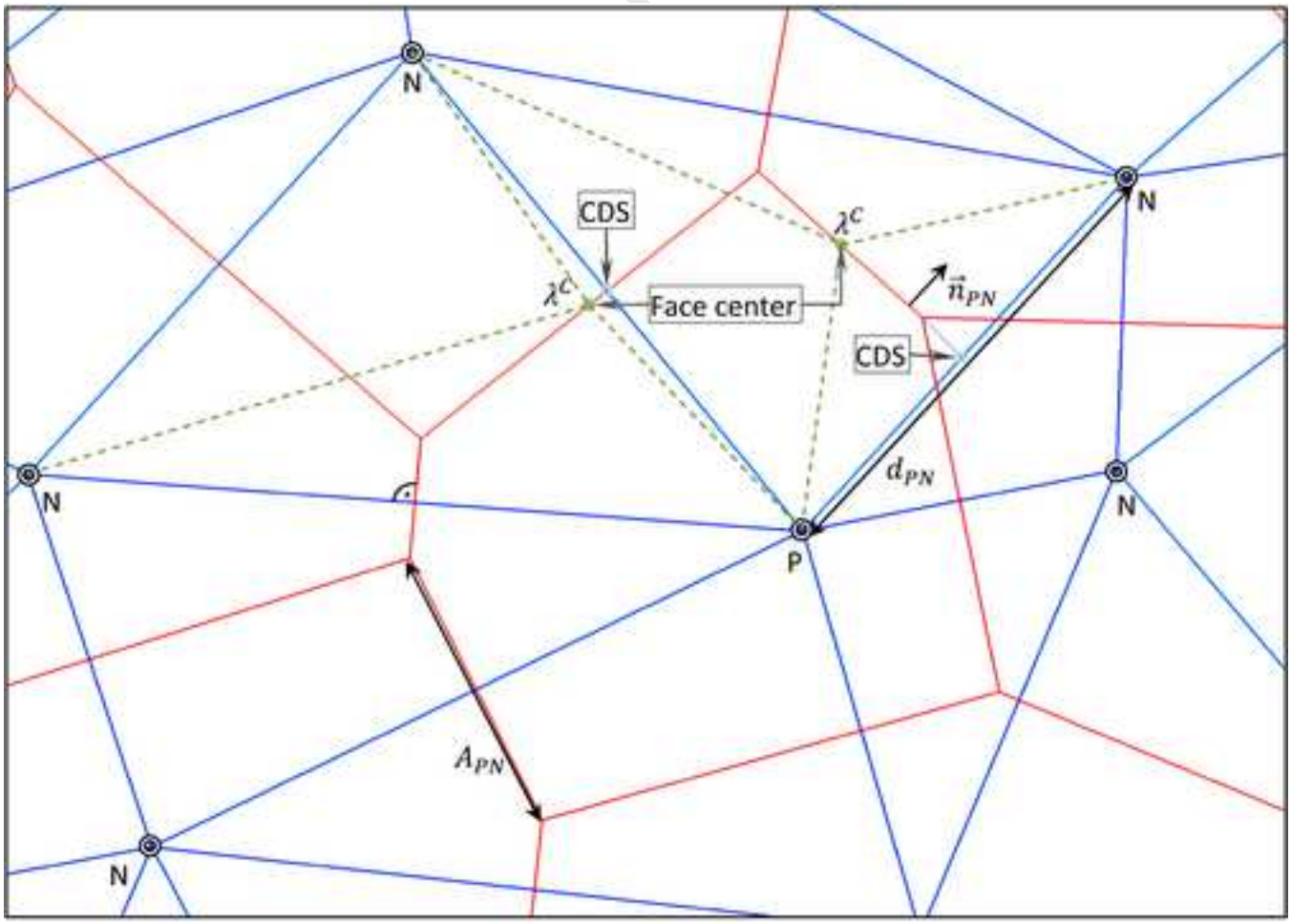

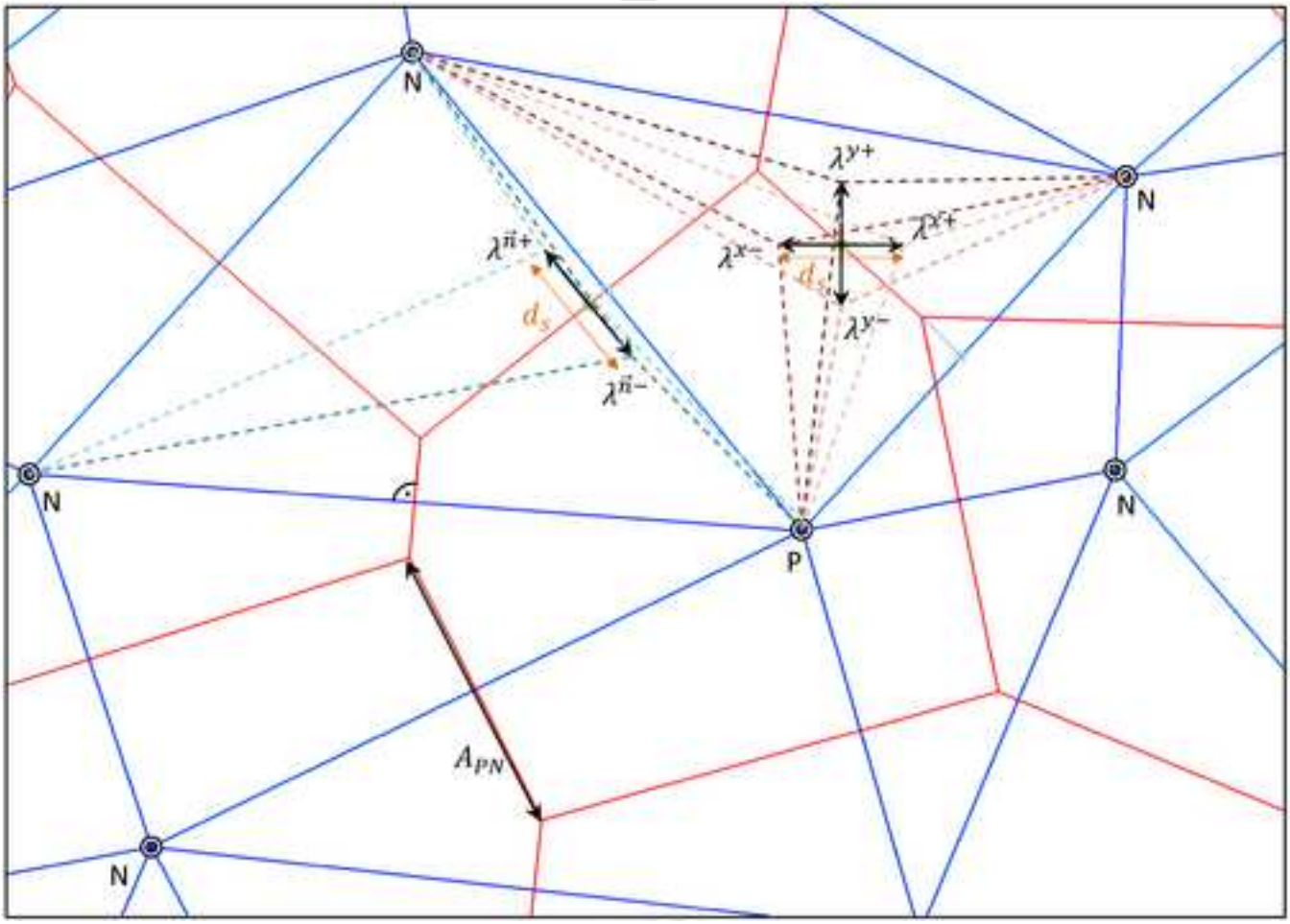

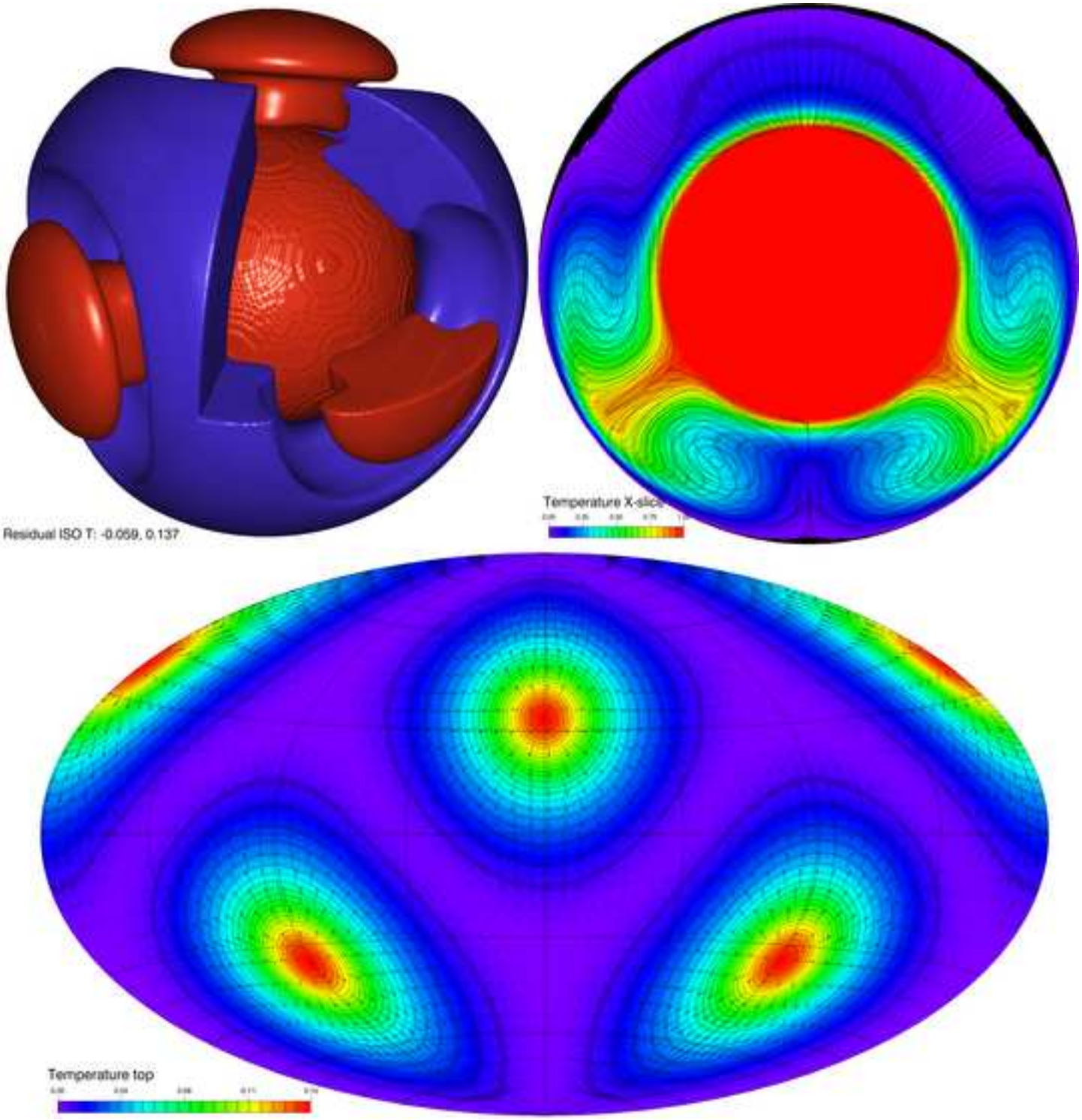

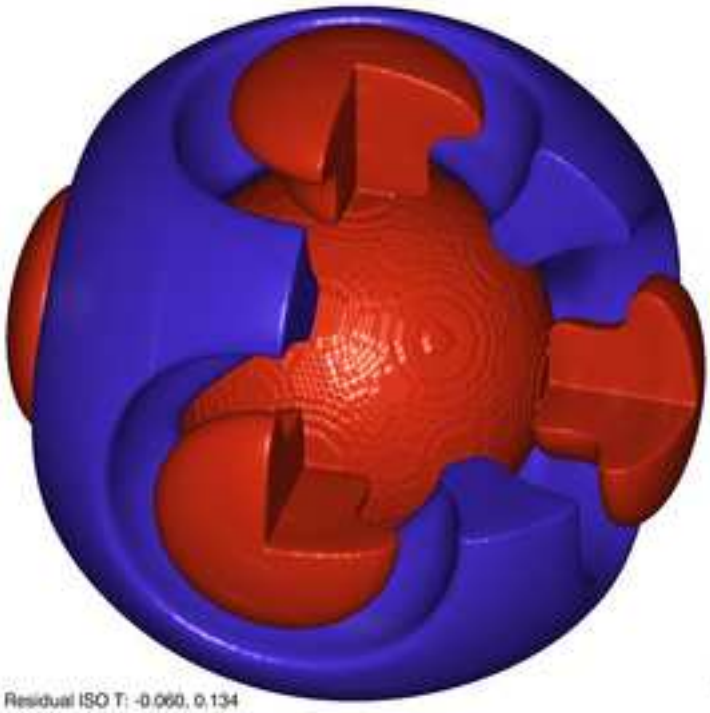

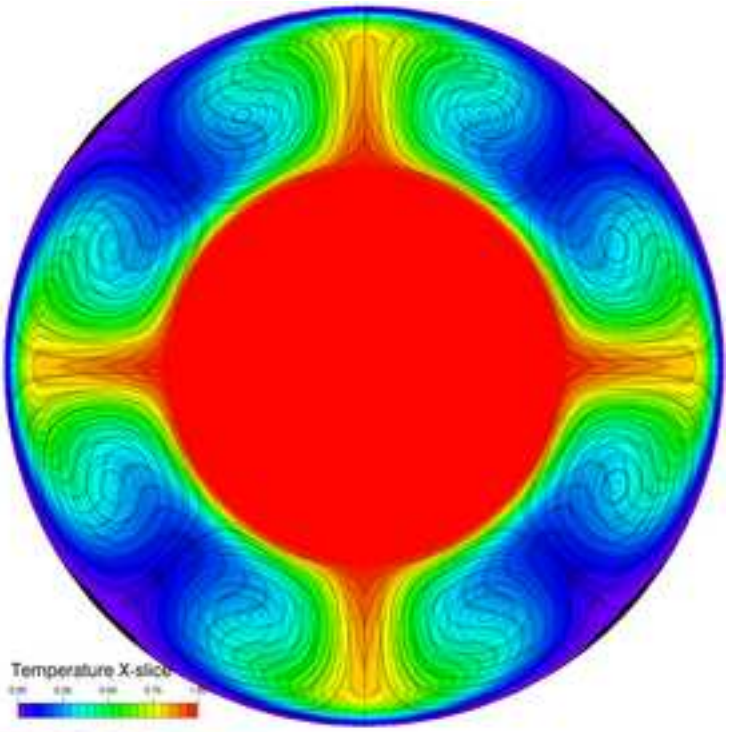

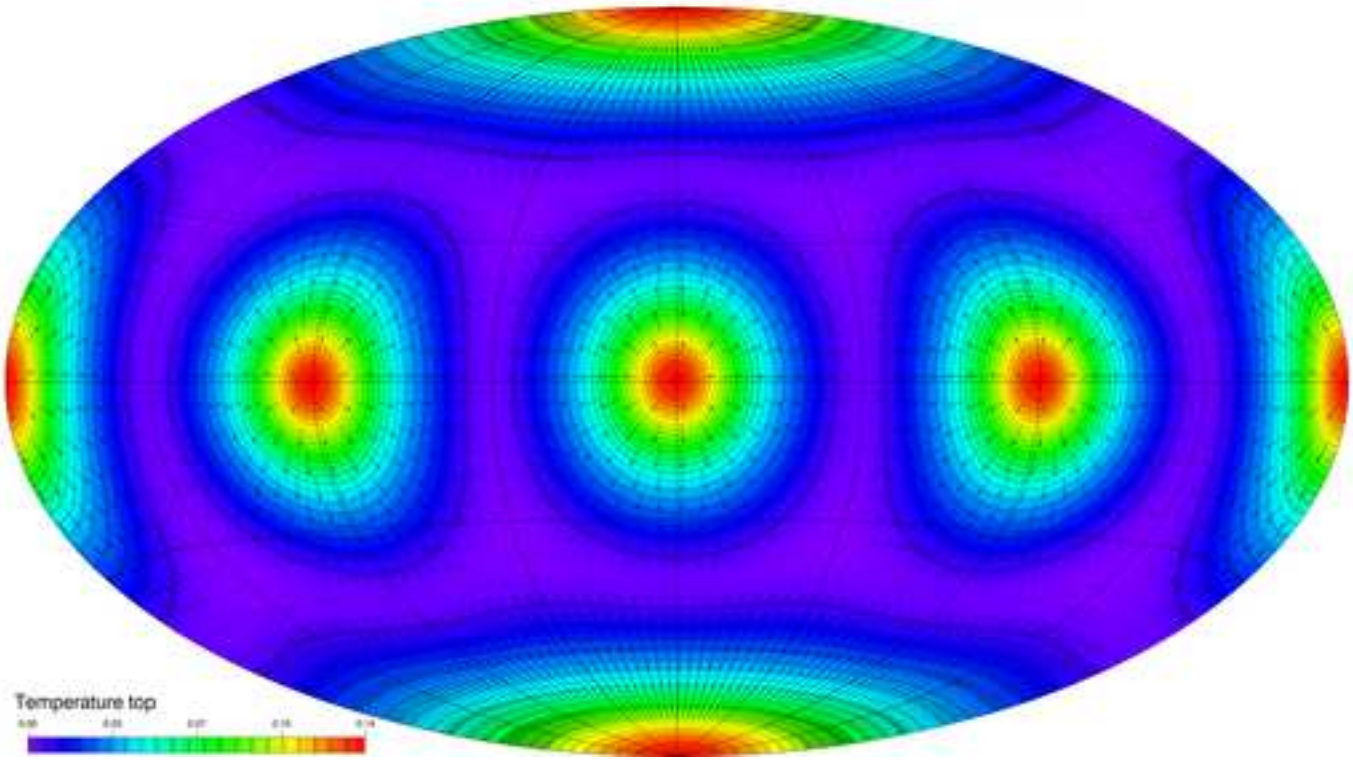

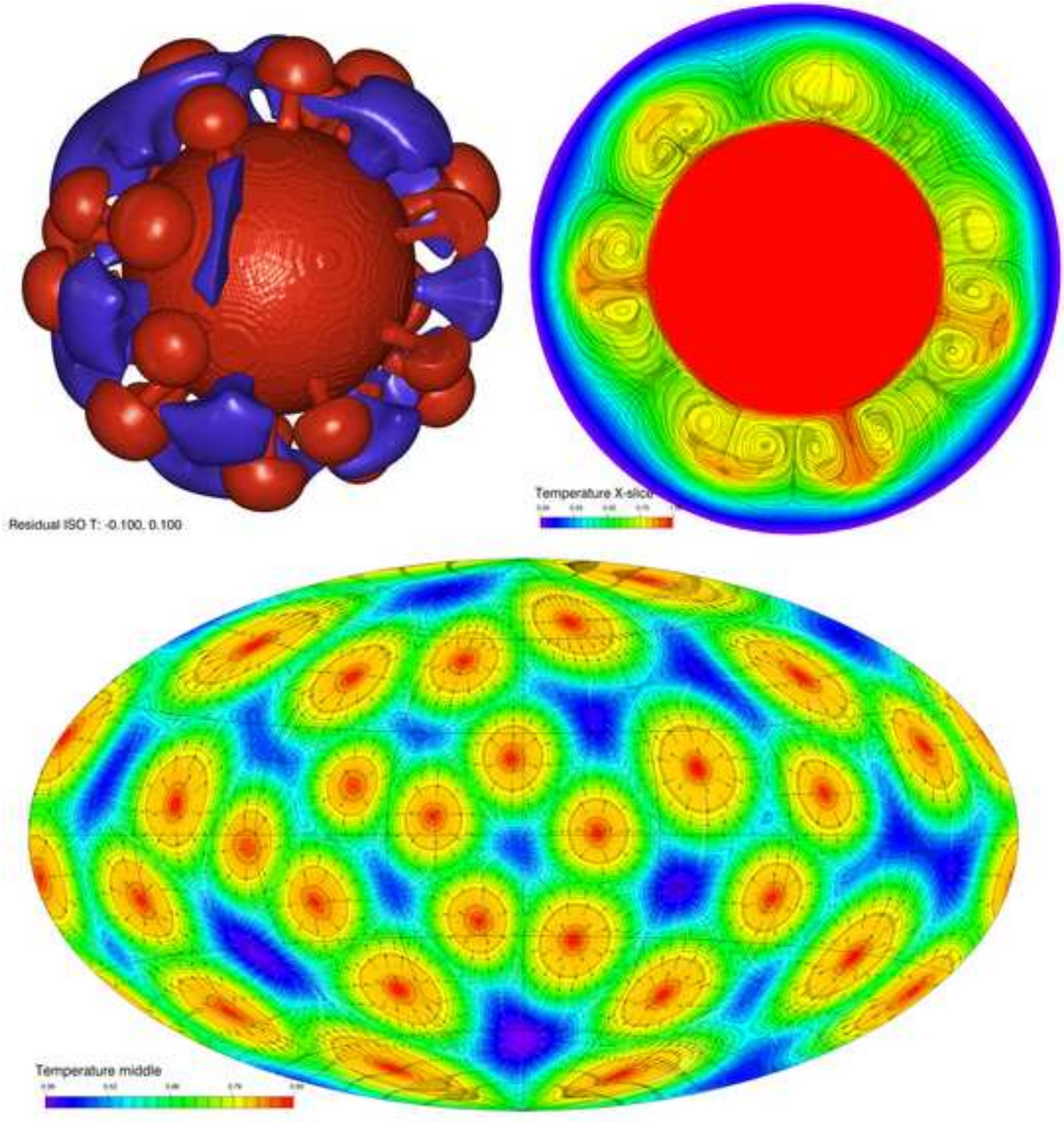

Figure 6a

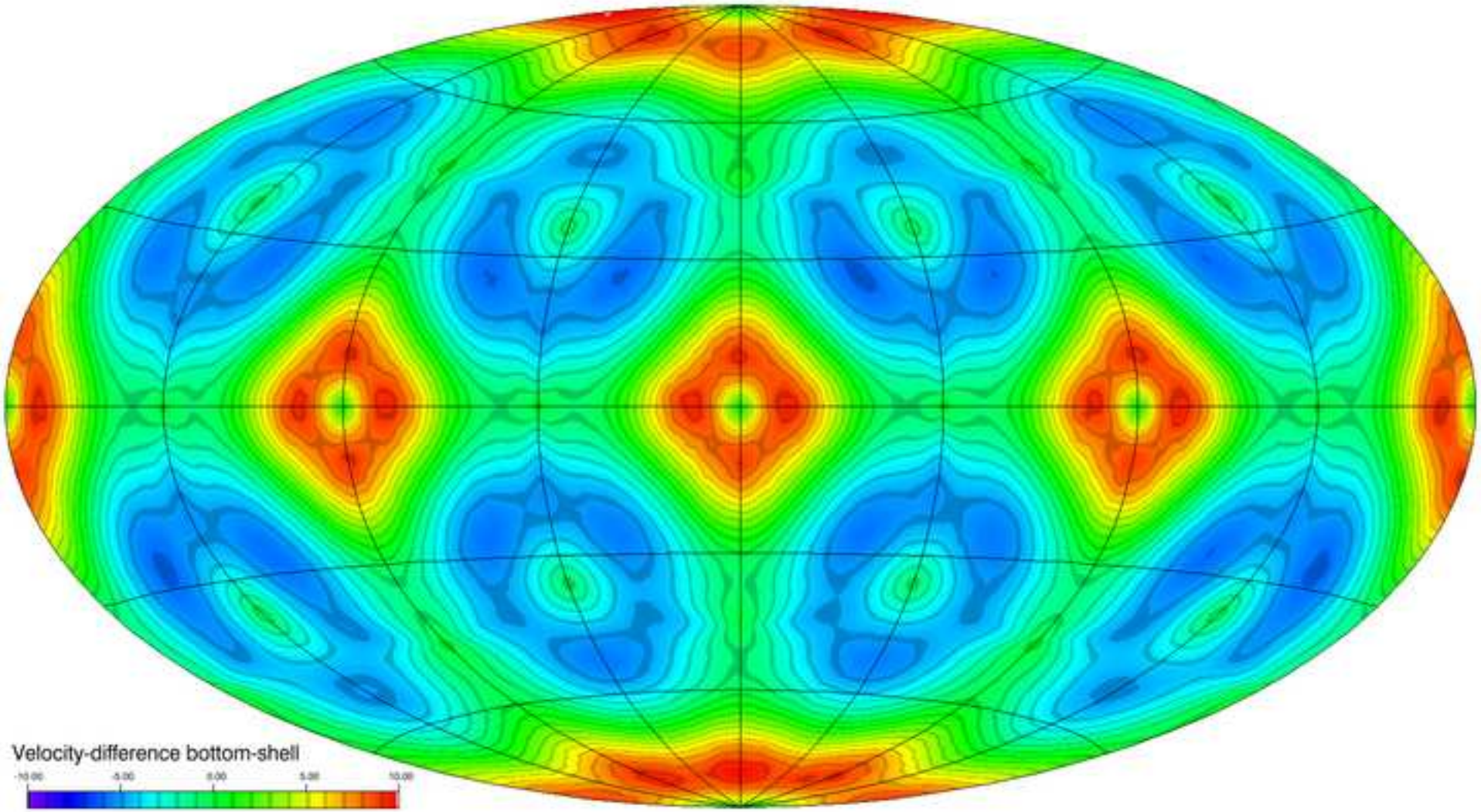

Figure 6b

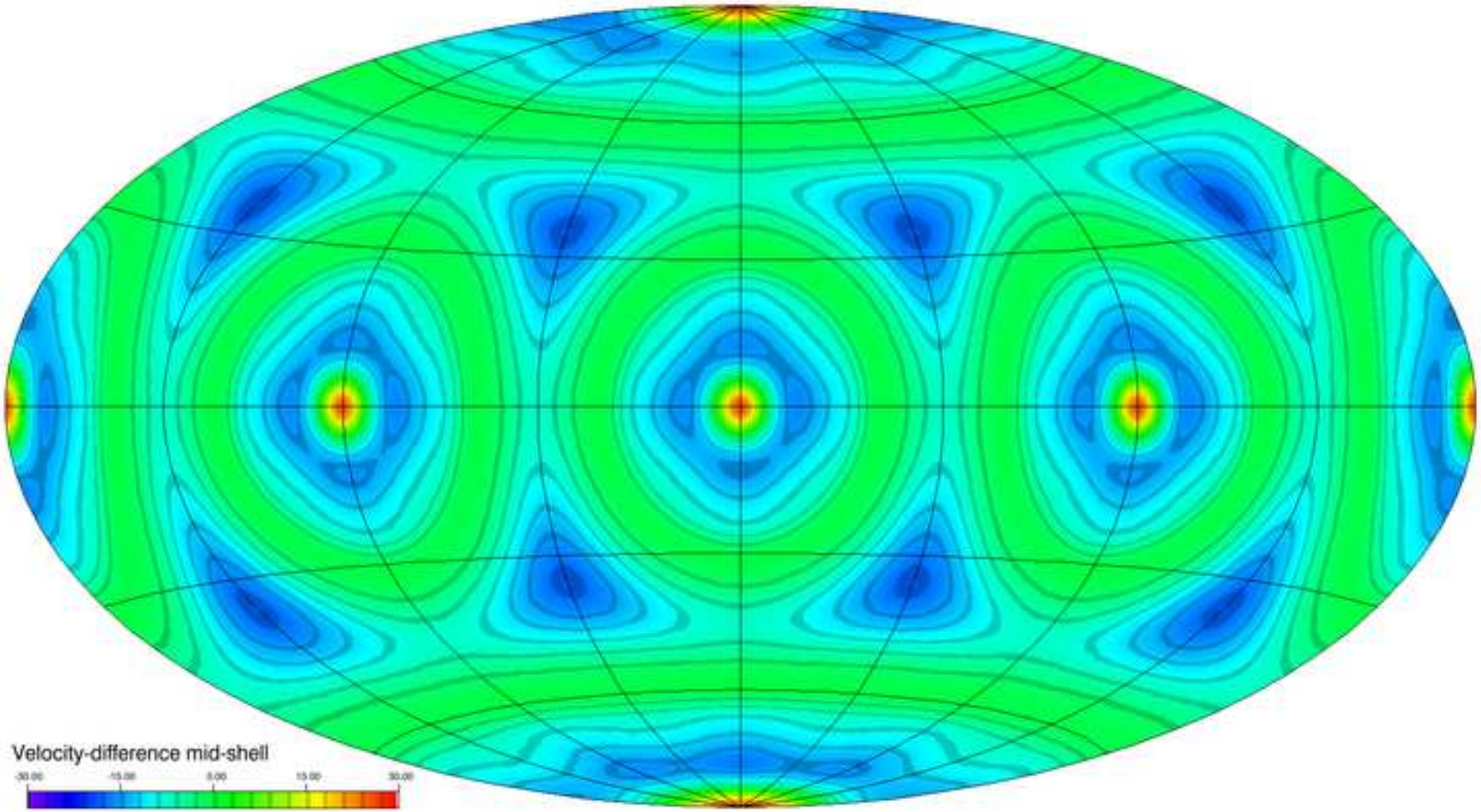

Figure 6c